A universal and scalable transformation of bulk metals into single-atom catalysts in ionic liquids

Wang, Shujuan; Lu, Minghui; Xia, Xuewen; Wang, Fei; Xiong, Xiaolu; Ding, Kai; Pang, Zhongya; Li, Guangshi; Xu, Qian; Hsu, Hsien-Yi; Hu, Shen; Ji, Li; Zhao, Yufeng; Wang, Jing; Zou, Xingli; Lu, Xionggang

Published in:
PNAS: Proceedings of the National Academy of Sciences of the United States of America

Published: 05/03/2024

Document Version:
Final Published version, also known as Publisher's PDF, Publisher's Final version or Version of Record

Published version (DOI):
10.1073/pnas.2319136121

Publication details:
Wang, S., Lu, M., Xia, X., Wang, F., Xiong, X., Ding, K., Pang, Z., Li, G., Xu, Q., Hsu, H.-Y., Hu, S., Ji, L., Zhao, Y., Wang, J., Zou, X., & Lu, X. (2024). A universal and scalable transformation of bulk metals into single-atom catalysts in ionic liquids. *PNAS: Proceedings of the National Academy of Sciences of the United States of America*, *121*(10). https://doi.org/10.1073/pnas.2319136121

PNAS RESEARCH ARTICLE | CHEMISTRY

A universal and scalable transformation of bulk metals into single-atom catalysts in ionic liquids

Shujuan Wang[a,b,1], Minghui Lu[a,1], Xuewen Xia[a,1], Fei Wang[a], Xiaolu Xiong[b], Kai Ding[a], Zhongya Pang[a], Guangshi Li[a], Qian Xu[a], Hsien-Yi Hsu[c], Shen Hu[d], Li Ji[d,2], Yufeng Zhao[e,2], Jing Wang[f], Xingli Zou[a,2], and Xionggang Lu[a]

Edited by Alexis Bell, University of California, Berkeley, CA; received November 1, 2023; accepted January 17, 2024

Single-atom catalysts (SACs) with maximized metal atom utilization and intriguing properties are of utmost importance for energy conversion and catalysis science. However, the lack of a straightforward and scalable synthesis strategy of SACs on diverse support materials remains the bottleneck for their large-scale industrial applications. Herein, we report a general approach to directly transform bulk metals into single atoms through the precise control of the electrodissolution–electrodeposition kinetics in ionic liquids and demonstrate the successful applicability of up to twenty different monometallic SACs and one multimetallic SAC with five distinct elements. As a case study, the atomically dispersed Pt was electrodeposited onto Ni_3N/Ni-Co-graphene oxide heterostructures in varied scales (up to 5 cm × 5 cm) as bifunctional catalysts with the electronic metal–support interaction, which exhibits low overpotentials at 10 mA cm^{-2} for hydrogen evolution reaction (HER, 30 mV) and oxygen evolution reaction (OER, 263 mV) with a relatively low Pt loading (0.98 wt%). This work provides a simple and practical route for large-scale synthesis of various SACs with favorable catalytic properties on diversified supports using alternative ionic liquids and inspires the methodology on precise synthesis of multimetallic single-atom materials with tunable compositions.

single-atom catalysts | electrodissolution–electrodeposition | ionic liquids | HER/OER

Significance

Atomically dispersed metal catalysts, including monometallic and multimetallic single-atom catalysts (SACs), still face certain challenges, i.e., general and scalable synthesis process, compatibility with various support materials, etc. This work proposed a general electrodissolution–electrodeposition strategy in alternative ionic liquids media to convert bulk metals into dispersed atoms. Twenty different monometallic SACs and one multimetallic SAC with five distinct elements have been synthesized on different support materials, the synthesized Pt-SAC exhibits excellent catalytic performance for alkaline hydrogen evolution reaction and oxygen evolution reaction. This work provides an insight into the accurate control of the single-atom electrodeposition kinetics, which has excellent promise to serve as a general strategy for the electrosynthesis of SACs for various applications.

Exploiting sustainable energy resources and developing low-carbon technologies are critical for resolving the emerging energy crisis and are the pathway toward a society with carbon neutrality (1, 2). Single-atom catalysts (SACs) with isolated metallic atoms anchored on supports have received soaring scientific interest global-wide in recent years, exhibiting tremendous catalytic capabilities for various catalysis reactions, such as hydrogen evolution reaction (HER), oxygen evolution reaction (OER), nitrogen reduction reaction (NRR), CO_2 reduction reaction (CO_2RR), etc. (3–5). Numerous strategies have been proposed to produce versatile SACs, such as wet chemistry, atomic layer deposition, chemical vapor deposition, etc. (6–8) (*SI Appendix*, Fig. S1). In particular, some pioneering efforts have recently focused on exploring a universal and straightforward strategy to achieve the mass production of SACs and even multimetallic SACs. For instance, a gas-migration strategy was put forward to directly transform bulk metals into single atoms (SAs) on nitrogen-doped carbon (N-C) supports and demonstrated with three different metals (M-SAs/N-C, M = Cu, Ni, Co) (7). After that, an extensive library of monometallic SACs with 37 different metallic elements and multimetallic SACs, such as 2-, 8- and 12-metal SACs, were realized using a dissolution-and-carbonization synthesis method (9). In 2023, Zou et al. reported a laser-planting strategy to synthesize several SACs including a multiple metallic (e.g., PtIrCuCoNi) (10). However, the practical applications of SACs remain hindered due to the strict requirements and tedious synthesis steps (e.g., high-temperature treatment) in the synthesis process, as well as the substantial gap between lab-scale demonstrations and industrial-scale utilization with high affordability. More importantly, the precise control of the interactions between SAs and supports remains the bottleneck for the large-scale synthesis of monometallic SACs as well as constructing SACs with multimetallic centers for their diversified applications.

Electrochemical methods show advantages of simple operation and promising expansibility for industrial applications and have recently been applied to prepare various SACs (*SI Appendix*, Table S1), including Ru_1/D-NiFe LDH (11), Pt/np-$Co_{0.85}Se$ (12), C-Ir_1/$Co_{0.8}Fe_{0.2}Se_2$ (13), Pt_{SA}-$Co(OH)_2$@Ag NW (14), etc. Nevertheless, most of these works generally utilize salt-precursors [e.g., H_2PtCl_6 (15)] and share the same issues in manipulating the electrodeposition kinetics due to the instantaneous concentration variation of metal ions and the rapid nucleation of metal nuclei (16). Meanwhile, the prevailing electrochemical synthesis of SACs with aqueous solutions as electrolytes was limited by the intrinsic properties (e.g., narrow electrochemical windows), which excludes the applicability for versatile metals (e.g., W, Mg, Al, etc.). Additionally, the electrochemical process in

Author contributions: S.W. and X.Z. designed research; S.W., M.L., and X. Xia performed research; S.W., F.W., X. Xiong, K.D., Z.P., G.L., Q.X., H.-Y.H., S.H., J.W., and X.L. analyzed data; and S.W., L.J., Y.Z., and X.Z. wrote the paper.

The authors declare no competing interest.

This article is a PNAS Direct Submission.

[1]S.W., M.L., and X. Xia contributed equally to this work.

[2]To whom correspondence may be addressed. Email: lji@fudan.edu.cn, yufengzhao@shu.edu.cn, or xlzou@shu.edu.cn.

This article contains supporting information online at https://www.pnas.org/lookup/suppl/doi:10.1073/pnas.2319136121/-/DCSupplemental.

Published February 26, 2024.

aqueous electrolytes is commonly accompanied by hydrogen evolution, resulting in inevitable cathode metal embrittlement (17, 18) and metal agglomerations triggered by the surface blocking effect (19, 20). Therefore, a universal and scalable electrochemical synthesis strategy for SACs should allow the accurate control of the single-atom deposition kinetics, whereby electrolytes with moderate electrochemical reaction rates and wide electrochemical windows are required to achieve generality and homogeneousness.

In this work, we report a simple electrochemical strategy that enables direct transformation of various bulk metals into SACs in ionic liquid electrolytes [e.g., the choline chloride–ethylene glycol (ethaline)] via an in situ electrodissolution–electrodeposition route, whereby the wide electrochemical window, excellent stability, and adjustable viscosity of ionic liquids (21) offer an exciting access to the controllable generation of diverse SAs. As case studies, 20 bulk metals (Mg, Al, V, Cr, Mn, Fe, Co, Ni, Cu, Zn, Mo, Ru, In, Sn, W, Ir, Pd, Ag, Pt, and Au) have been successfully transformed into SAs, and a multimetallic SAC with 5 different elements, i.e., Co, Ni, Ir, Pt, and Au (5-metal SAC) has also been realized. Among them, single Pt atoms (0.98 wt% loading) have been incorporated into Ni_3N/Ni-Co-graphene oxide (GO) heterostructure composite supported by carbon cloth (Pt_{SA}-Ni_3N/Ni-Co-GO@CC). The resultant catalyst with the electronic metal–support interaction modulation exhibits prominent bifunctional electrocatalysis activity in alkaline media, with ultralow overpotentials of 30 mV for HER and 263 mV for OER to achieve a current density of 10 mA cm^{-2}. A two-electrode electrolyzer was directly assembled using the self-supported Pt_{SA}-Ni_3N/Ni-Co-GO@CC electrodes for overall water splitting, exhibiting excellent stability over 200 h. Moreover, the scaling capability was demonstrated by preparing a 5 cm × 5 cm catalytic electrode. Intriguingly, the proposed strategy can also be adapted to diverse supports and ionic liquids systems, which suggests that it can be extended to prepare various monometallic and multimetallic SACs with favorable catalytic properties toward multifunctional applications.

Results

Synthesis Strategy and Construction Mechanism of SACs. Generally, electrodeposition of SACs in liquid electrolytes requires an equilibrium electrochemical process to achieve the atomic-scale control of SAs formation, suggesting that an in situ electrodissolution–electrodeposition process may offer access for accurately fabricating SACs. However, it still remains challenges to produce SACs directly from bulk metals in aqueous electrolytes since their limited in situ electrodissolution reactions. Ionic liquids generally hold a wide potential window (2.0 to 5.8 V) (22, 23) and viscosity range (20 to 40,000 cP) (24), providing possibilities to control metal electrodisslution, ion diffusion, and metal electrodeposition kinetics during the electrochemical process (25, 26), and thus facilitating the subtly regulation of single-atom materials formation (Fig. 1*A*). Besides, ionic liquids can provide electrostatic protection against aggregation, which have been proven to be effective in improving the stability of metal nanoparticles and homogeneous/single-site catalysts on the supports (27). Here, a halogen-containing deep eutectic solvent (DES, ethaline) with low cost, proper viscosity (52 cP for ethaline vs. 1 cP for water at 20 °C) (28) and wide electrochemical window (~2.0 V vs. ~1.23 V for water) (29) was selected as the electrolyte for SACs production. The halide ions (e.g., Cl^-) can promote the electrochemical dissolution of bulk metal, as evidenced in our recent work (30), while the moderate viscosity can also guarantee a suitable metal ion transportation velocity for precisely tuning preferred kinetics. These key features highlight that the designed equilibrium electrodissolution–electrodeposition process in ionic liquids holds excellent promise to serve as a general approach for the electrochemical synthesis of SACs (Fig. 1*B*).

The electrodeposition of Pt SAs on a Ni_3N/Ni-Co-GO@CC support was initially selected to verify the applicability of the as-proposed strategy. Specifically, Ni-Co with embedded GO sheets was grown on CC substrate by electrodeposition in ethaline, followed by nitridation to form a Ni_3N/Ni-Co-GO@CC support for Pt SAs anchoring (Fig. 1*C* and *SI Appendix*, Figs. S2 and S6). The in situ electrodissolution–electrodeposition was conducted by cyclic voltammetry (CV) technology, with the prepared Ni_3N/Ni-Co-GO@CC electrode as the working electrode, a Pt foil counter electrode used as the bulk Pt metal precursor, and a nonaqueous Ag wire electrode as the reference electrode. During the electrochemical process, ethaline provides sufficient Cl^- surroundings to promote the anodic dissolution of bulk Pt counter electrode into the electrolyte, forming $PtCl_4^{2-}$ and $PtCl_6^{2-}$ (*SI Appendix*, Figs. S7 and S8). Ni/Co atoms are also slightly dissolved into ethaline, creating specific Ni/Co vacancies (*SI Appendix*, Fig. S9). Simultaneously, the Pt complex ions tardily electromigrate to the cathode surface region where they were electrodeposited and fixed by vacancy sites, and eventually produce desired Pt SACs (Pt_{SA}-Ni_3N/Ni-Co-GO@CC) with tunable loadings (0.18 to 1.12 wt%) controlled by regulating CV cycles (Fig. 1*D* and *SI Appendix*, Figs. S10 and S11). A scaled-up process was also demonstrated by increasing electrode sizes from 1 cm × 1 cm up to 5 cm × 5 cm, as shown in Fig. 1*D*. It is experimentally indicated that the in situ electrodissolution–electrodeposition process in ethaline can ensure the continuous Pt dissolution and stable redeposition simultaneously, which implies that the electrochemical process can reach optimum equilibrium electrodeposition for the synthesis of SACs. By simply changing the counter electrode, i.e., using different bulk metals as precursors, the proposed strategy can be facilely extended to produce various monometallic and multimetallic single-atom materials. In this work, Mg, Al, V, Cr, Mn, Fe, Co, Ni, Cu, Zn, Mo, Ru, In, Sn, W, Ir, Pd, Ag, and Au single-atom materials, as well as a multimetallic SAC, i.e., 5-metal SAC (Co, Ni, Ir, Pt, and Au) were achieved.

To explore the electrochemical synthesis process of SACs in ionic liquids, the electrodeposition of Pt on the same support material (Ni_3N/Ni-Co-GO@CC) was also carried out in several typical aqueous electrolytes [i.e., 1.0 M PBS (phosphate buffer solution), 1.0 M KOH, 1.0 and 5.0 M NaCl solutions] for comparison (*SI Appendix*, Figs. S12 and S14 and Movies S1–S5). The electrodeposition process of Pt in aqueous electrolytes was always accompanied by hydrogen evolution, whereby the insulating hydrogen bubbles would reduce the efficient active surface for anchoring metal atoms (17, 18) (*SI Appendix*, Fig. S15), and thus may easily cause agglomeration of SAs. Compared with PBS, KOH, and NaCl (including 1.0 and 5.0 M) electrolytes, the ethaline electrolyte also shows obvious superiority for in situ Pt electrodissolution (*SI Appendix*, Fig. S16). Additionally, uneven microstructures and formation of Pt clusters commonly occurred at the cathode in aqueous electrolytes, which is relatively hard to achieve precise control (*SI Appendix*, Figs. S17 and S18). To further understand the difference in the electrochemical processes, the electrochemical reduction behaviors of Pt ions in aqueous and ethaline electrolytes were further studied by CV. For the electrolytes with the same concentration of Pt species (K_2PtCl_4, 0.048 M), the reduction of Pt(II) in ethaline is diffusion-controlled with a diffusion coefficient of 1.44×10^{-6} cm^2 s^{-1} (*SI Appendix*, *Supporting Text 1*), which is two to three orders of magnitude lower

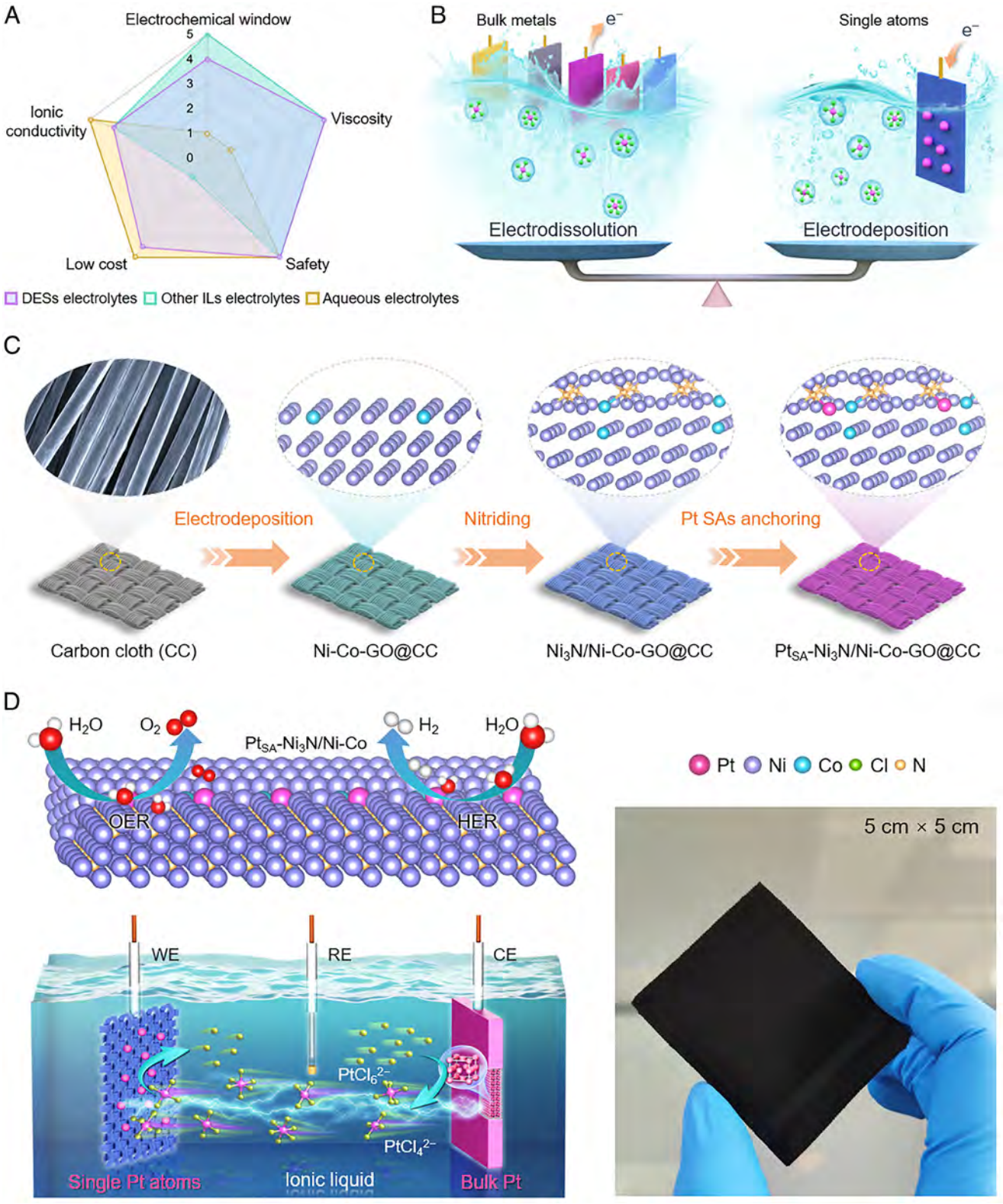

Fig. 1. Schematic representation of the strategy for synthesizing SACs and their mechanisms. (*A*) Radar plots of the properties of ionic liquid electrolytes (deep solvent eutectic and other ionic liquid electrolytes) and aqueous electrolytes. The values range from 0 (the center) to 5, where 5 means the highest value of a property, based on the reported works (29, 31, 32). (*B*) Schematic of the designed equilibrium relationship between the electrodissolution of bulk metals and the electrodeposition of SAs. (*C*) The illustration of the fabrication route for the self-supported Pt_{SA}-Ni_3N/Ni-Co-GO on CC substrate. (*D*) The illustration of the electrolytic synthesis mechanism of SACs as a catalyst for overall water splitting and the digital photo of the synthesized Pt_{SA}-Ni_3N/Ni-Co-GO (5 cm × 5 cm).

than that in conventional solvents (i.e., aqueous, organic solvents) (26, 33). While in the aqueous electrolyte, this process is controlled by electron transfer rates (*SI Appendix*, Fig. S19), implying that Pt ions have relatively slower transport kinetic processes in ethaline (26), and accordingly the electrochemical reaction speed in ionic liquids is commonly slower than that in aqueous electrolytes (25), which may contribute to avoiding the atoms aggregation caused by the fast migration of metal ions and the rapid

nucleation as well as the growth of nuclei. Furthermore, the electrostatic double layer generated by ionic liquids can maintain the stability of the electrocatalysts, which also cannot be achieved in aqueous solutions (27, 34). These results suggest that the in situ electrodissolution–electrodeposition process in ionic liquids can serve as an alternative strategy for synthesizing SACs.

Atomic Structure Characterization. The atomic-resolution high-angle annular dark-field scanning transmission electron microscopy (HAADF-STEM) and energy-dispersive spectroscopy (EDS) images (Fig. 2 and *SI Appendix*, Figs. S20 and S40) confirm that a family of monometallic SAs (including Mg, Al, V, Cr, Mn, Fe, Co, Ni, Cu, Zn, Mo, Ru, In, Sn, W, Ir, Pd, Ag, Pt, and Au), as well as multimetallic SAs containing five metal elements (Co, Ni, Ir, Pt, and Au with total metals loading of ~0.46 wt%), were atomically dispersed on different supports, including the Ni_3N/Ni-Co-GO, N-doped graphene (NG), NiCo layered double hydroxide, and $Ti_3C_2T_x$ MXene supports. The results of X-ray diffraction (XRD), X-ray photoelectron spectroscopy (XPS), X-ray absorption near-edge structure (XANES) spectroscopy, Fourier-transformed extended X-ray absorption fine structure (FT-EXAFS) and corresponding fittings also demonstrate that the successful construction of SACs (*SI Appendix*, Figs. S20, S38, S40, and S41 and Table S2). These results indicate that this method is universal and flexible for synthesizing various monometallic (*SI Appendix*, Fig. S42) and multimetallic SACs by selecting appropriate bulk metal electrodes, ionic liquids systems (*SI Appendix*, Fig. S39) as well as support materials (*SI Appendix*, Fig. S40).

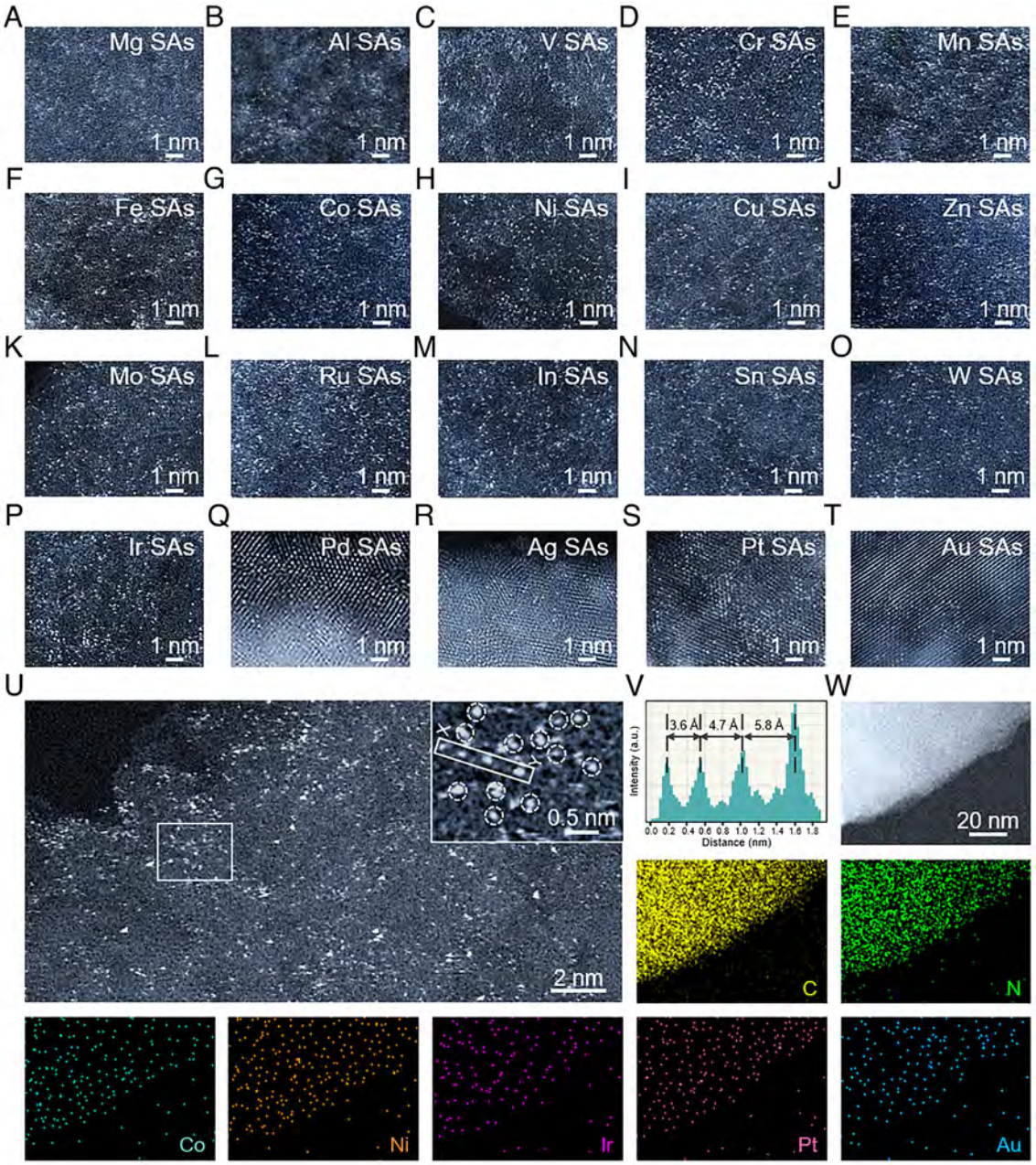

Fig. 2. Structural characterization of the SAs. HAADF-STEM images of Mg (*A*), Al (*B*), V (*C*), Cr (*D*), Mn (*E*), Fe (*F*), Co (*G*), Ni (*H*), Cu (*I*), Zn (*J*), Mo (*K*), Ru (*L*), In (*M*), Sn (*N*), W (*O*), and Ir (*P*) SAs supported on NG, and Pd (*Q*), Ag (*R*), Pt (*S*), Au (*T*) SAs supported on Ni_3N/Ni-Co-GO obtained in ethaline. (*U*) HAADF-STEM image of 5-metal SAC (Co, Ni, Ir, Pt, and Au) supported on NG. The *Inset* is the close-up view of the boxed area, and the white circles mark the isolated metal atoms. (*V*) Line-scanning intensity profile along X-Y in the region highlighted with white rectangles in the *Inset* of (*U*). (*W*) HAADF-STEM image of 5-metal SAC and its corresponding EDS elemental maps.

Systematical characterizations were performed on the typically produced Pt_{SA}-Ni_3N/Ni-Co-GO to analyze the structural information of the as-obtained SACs. The X-ray diffraction (XRD) patterns of the synthesized Pt_{SA}-Ni_3N/Ni-Co-GO and Pt_{SA}-Ni_3N-Co-GO show no prominent characteristic peaks of Pt metal except for light shifts (*SI Appendix*, Fig. S43), elucidating that atomic-level Pt is doped into the phases (Ni_3N/Ni-Co and Ni_3N-Co) and nicely incorporated into the original crystal lattice (12, 35). Additionally, a phase interface of the Pt_{SA}-Ni_3N/Ni-Co-GO can be further determined through transition electron microscopy (TEM) and high-resolution TEM (HRTEM) images (*SI Appendix*, Figs. S44 and S45), and the salient interplanar distances of 0.157 and 0.203 nm on both sides of the interface can be ascribed to the (112) and (111) planes of the hexagonal Ni_3N as well as the cubic Ni phase, respectively (36, 37), which confirms the formation of Ni_3N/Ni heterostructure with Co incorporating. Isolated Pt atoms (circled) were manifested by the HAADF-STEM analysis (Fig. 3 *A* and *D*), whereby the heavy constituent atoms (bright spots) can be found to be commendably dispersed in the crystal lattice of Ni_3N/Ni-Co and primarily concentrated at the phase interface, implying that Pt SAs are immobilized at Ni/Co positions (38–40). Besides, the different line intensity profiles of two typical areas show the loosely interatomic distances between bright spots, which also confirms the isolated Pt atoms (Fig. 3*B*). As a comparison, Pt SAs were also fixed in Ni_3N-Co-GO catalyst without heterostructure by the same method (*SI Appendix*, Fig. S46*A*). The elemental mapping images further demonstrate the homogeneous distribution of Pt atoms throughout the synthesized Pt_{SA}-Ni_3N/Ni-Co-GO and Pt_{SA}-Ni_3N-Co-GO catalysts (Fig. 3*D* and *SI Appendix*, Fig. S46*B*).

The XANES spectra display that the white-line intensity of Pt_{SA}-Ni_3N/Ni-Co-GO is lower than that of PtO_2 but higher than that of Pt foil (Fig. 3*E*), affirming that Pt atoms in Pt_{SA}-Ni_3N/Ni-Co-GO are more positive ($Pt^{\delta+}$) in oxidation state relative to Pt foil (Pt^0), which may be attributed to the electron transfer from Pt to the Ni_3N/Ni-Co-GO support. Moreover, the FT-EXAFS oscillations for the Pt_{SA}-Ni_3N/Ni-Co-GO shown in Fig. 3F, one conspicuous peak at ~1.7 Å can be ascribed to Pt-N coordination. There is no Pt-Pt contribution of Pt foil at ~2.6 Å (metallic bonding), suggesting no Pt particles or clusters formation. Additionally, the first-shell fitting results from FT-EXAFS features give the coordination number (CN) of approximately 2.0 for the Pt-N shell, 0.6 for Pt-Ni shell or Pt-Co shell in Pt_{SA}-Ni_3N/Ni-Co-GO (*SI Appendix*, Figs. S46 *B* and *D* and Table S2). It is suggested that the Pt atoms coordinate with N and Ni/Co atoms, occupying the interfacial and superficial Ni or Co positions in the lattice of Ni_3N/Ni-Co. The Ni and Co K-edge XANES spectra of Ni_3N/Ni-Co-GO and Pt_{SA}-Ni_3N/Ni-Co-GO show similar but slightly different adsorption features (*SI Appendix*, Fig. S48 *A* and *C*). Compared with Ni_3N/Ni-Co-GO, the higher intensity white-line peak of Pt_{SA}-Ni_3N/Ni-Co-GO verifies the local atomic arrangement of Ni or Co atoms originating from the Pt SAs anchoring. For the FT-EXAFS spectra (*SI Appendix*, Fig. S48 *B* and *D*), the significant peaks of Pt_{SA}-Ni_3N/Ni-Co-GO shift to a higher value of 0.06 and 0.04 Å compared to that of Ni_3N/Ni-Co-GO, respectively, which might be attributed to the structural lattice distortion caused by the substitution doping of Pt SAs. As displayed in Fig. 3*G*, the wavelet transform (WT) contour maps in Pt L_3-edge illuminate that the location of the WT intensity maxima (~6.0 $Å^{-1}$, ~1.6 Å) for the Pt_{SA}-Ni_3N/Ni-Co-GO is different with that of PtO_2 (~5.1 $Å^{-1}$, ~1.5 Å) and Pt foil (~11.4 $Å^{-1}$, ~2.6 Å) in *k*- and *R*-spaces, respectively, verifying the existence of isolated Pt sites.

The XPS spectra (Fig. 3*H* and *SI Appendix*, Figs. S49 and S50) display that two characteristic signals (Pt $4f_{5/2}$ and $4f_{7/2}$) of the Pt_{SA}-Ni_3N/Ni-Co-GO exhibit a slight positive shift of 0.5 eV with respect to Pt/C indicated Pt^0, proving the presence of partially positive charged Pt atoms ($Pt^{\delta+}$), due to the strong interaction with charge-transfer between the single Pt atoms and the Ni_3N/Ni-Co-GO support (41). To dissect the dispersion of Pt, the CO adsorption over the fabricated Pt_{SA}-Ni_3N/Ni-Co-GO has also been investigated by in situ Fourier-transform infrared (FTIR) spectroscopy measurement (Fig. 3*I*). A narrow and quasi-symmetrical band appears at ~2,083 cm^{-1} during the CO desorption process, which can be rationally assigned to linearly absorbed CO on $Pt^{\delta+}$ single-atom sites, as commonly observed in Pt single-atom catalysts (42–45). These analyses prove that the separated Pt atoms are atomically decentralized in the Ni_3N/Ni-Co-GO. After anchoring isolated Pt atoms, the Pt_{SA}-Ni_3N/Ni-Co-GO catalyst exhibits enhanced absorption energy and conductivity (*SI Appendix*, Fig. S51), thus potentially promoting the electrocatalytic processes (46).

Electrocatalytic Performance Evaluation. The HER activities of the Pt_{SA}-Ni_3N/Ni-Co-GO catalysts obtained under different CV cycles, Pt_{SA}-Ni_3N-Co-GO, Ni_3N/Ni-Co-GO, Ni-Co-GO, 20 wt% Pt/C, and other 19 metal SACs were evaluated by linear sweep voltammetry (LSV) in 1.0 M KOH solution (Fig. 4 *A* and *C* and *SI Appendix*, Figs. S52 and S54 and Movie S6). Notably, the Pt_{SA}-Ni_3N/Ni-Co-GO catalyst obtained within 4000 CV cycles (only 0.98 wt% Pt SAs) displays the most remarkable catalytic performance, exhibiting overpotentials of 30 (η_{10}) and 61 mV (η_{100}) at the current densities of 10 and 100 mA cm^{-2}, respectively. Its overpotential is lower than those of 20 wt% Pt/C (η_{10} = 36 mV), Ni_3N/Ni-Co-GO (η_{10} = 78 mV), Pt_{SA}-Ni_3N-Co-GO (η_{10} = 87 mV), and Ni-Co-GO (η_{10} = 94 mV), demonstrating that the enhanced HER activity of Pt_{SA}-Ni_3N/Ni-Co-GO is mainly attributed to the efficient interaction between Pt SAs and the noncarbon support. Meanwhile, a Tafel slope (*b*) of 27.4 mV dec^{-1} for the Pt_{SA}-Ni_3N/Ni-Co-GO catalyst was also observed, which is significantly lower than those of Pt/C (28.5 mV dec^{-1}), wNi_3N/Ni-Co-GO (69.8 mV dec^{-1}), Pt_{SA}-Ni_3N-Co-GO (93.0 mV dec^{-1}), and Ni-Co-GO (78.8 mV dec^{-1}) (Fig. 4*B* and *SI Appendix*, Fig. S52*D*), unambiguously suggesting the rapid HER kinetics originated from the incorporation of isolated Pt atoms. Based on the *b* of 27.4 mV dec^{-1}, which is close to the *b* (30 mV dec^{-1}) of Tafel reaction (M-H + M-H → H_2 + 2M) (47), the H_2 generated by the Pt_{SA}-Ni_3N/Ni-Co-GO catalysis follows a Volmer-Tafel mechanism with the Tafel step (chemical desorption) as the rate-limiting step. Note that the unusual mass activity of this catalyst at an overpotential of 100 mV reaches 6.33 A mg^{-1}, nearly 58 times greater than that of Pt/C (0.11 A mg^{-1}) under the same conditions (Fig. 4*D* and *SI Appendix*, *Supporting Text 2*). Moreover, the turnover frequency (TOF) of Pt_{SA}-Ni_3N/Ni-Co-GO at −80 mV was calculated to be 5.65 H_2 s^{-1}, approximately 71 times higher than that of Pt/C (0.08 H_2 s^{-1}), indicating the highly efficient utilization of Pt SAs (Fig. 4*E* and *SI Appendix*, *Supporting Text 3*).

Apparently, the Pt_{SA}-Ni_3N/Ni-Co-GO catalyst exhibits ultralow overpotential and Tafel slope (η_{10} = 30 mV, *b* = 27.4 mV dec^{-1}), surpassing most of the reported state-of-the-art electrocatalysts obtained by diverse methods (Fig. 4*F* and *SI Appendix*, Tables S3 and S4), such as Pt@PCM (48) (η_{10} = 139 mV, *b* = 73.6 mV dec^{-1}), Pt_1/N-C (42) (η_{10} = 46 mV, *b* = 36.8 mV dec^{-1}), Pt SA/MXene (49) (η_{10} = 33 mV, *b* = 43.9 mV dec^{-1}). Its excellent HER catalytic activity is mainly attributed to the coordination species (N) with lone electron pairs, which can capture isolated

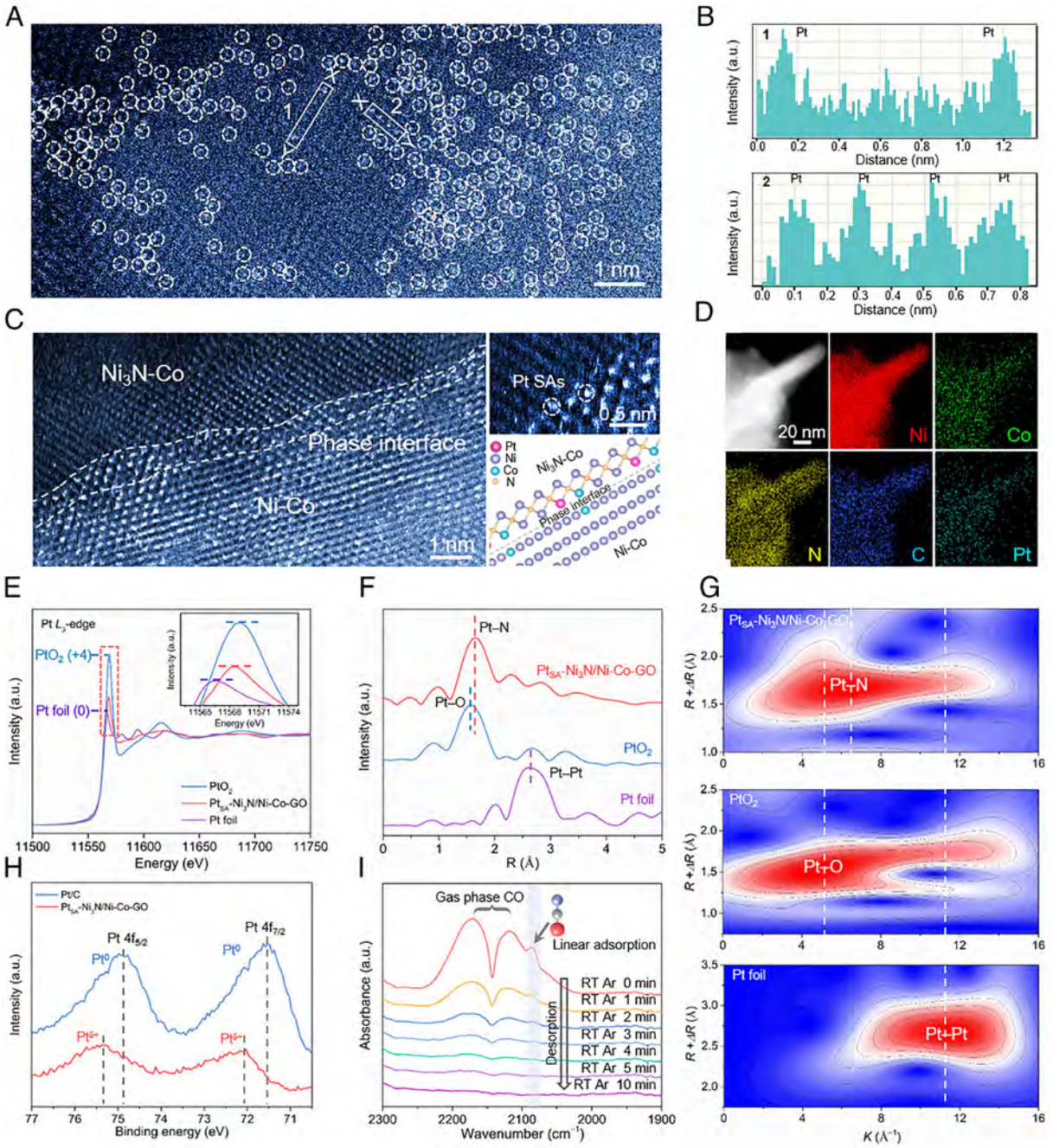

Fig. 3. Surface electronic state and atomic structure characterizations. (*A*) HAADF-STEM image of Pt_{SA}-Ni_3N/Ni-Co-GO and the isolated Pt atoms are marked by the white circles. (*B*) Line-scanning intensity profiles along X-Y in regions 1 and 2 highlighted with white rectangles in (*A*). (*C*) HAADF-STEM images of Pt_{SA}-Ni_3N/Ni-Co-GO with heterostructure and its corresponding interface structure constructed by DFT. (*D*) HAADF-STEM image and its corresponding EDS elemental mapping of Pt_{SA}-Ni_3N/Ni-Co-GO. (*E*) The normalized XANES spectra at Pt L_3-edge of Pt_{SA}-Ni_3N/Ni-Co-GO, Pt foil, and PtO_2. The *Inset* shows the corresponding local enlargement. (*F*) FT-EXAFS spectra corresponding to (*E*). (*G*) Wavelet transform contour spectra of PtO_2, Pt_{SA}-Ni_3N/Ni-Co-GO, and Pt foil. (*H*) XPS spectra of the Pt_{SA}-Ni_3N/Ni-Co-GO and commercial Pt/C in Pt 4f region. (*I*) In situ FTIR spectra of CO adsorption over the Pt_{SA}-Ni_3N/Ni-Co-GO.

Pt metal centers and regulate their electronic structures (50). Compared with the previously reported various SACs obtained by electrochemical methods in aqueous solutions (Fig. 4*G* and *SI Appendix*, Table S1), the Pt_{SA}-Ni_3N/Ni-Co-GO synthesized in ethaline exhibits comparable HER activity with relatively low Pt loading, which is also superior to the catalysts prepared in PBS, KOH, and NaCl aqueous solutions in this work (*SI Appendix*, Figs. S55–S57). Additionally, the maximum current density of the electrochemical synthesis process in ethaline for SACs is approximately 28 mA cm^{-2} (*SI Appendix*, Fig. S12*A*), much smaller than those of the reported synthesis processes in aqueous solutions (Fig. 4G, i.e., reaching up to 80 to 1,000 mA cm^{-2}) (12, 14, 51, 52), which is mainly created by the electrodeposition of Pt and the accompanied hydrogen evolution reaction. These results confirm that the reaction speed in ethaline for forming SAs has been slowed down, suggesting the electrochemical synthesis of SACs with tunable Pt loadings (*SI Appendix*, Figs. S52*B* and S56) can be facilely controlled in ionic liquids with slower kinetics. Notably, the Pt_{SA}-Ni_3N/Ni-Co-GO synthesized in ethaline has a mass activity of 6.33 A mg^{-1} with 0.98 wt% Pt, outperforming other reported Pt SACs obtained in aqueous solutions [e.g., the mass activity of 1.32 A mg^{-1} with 1.03 wt% Pt in Pt/np-$Co_{0.85}Se$

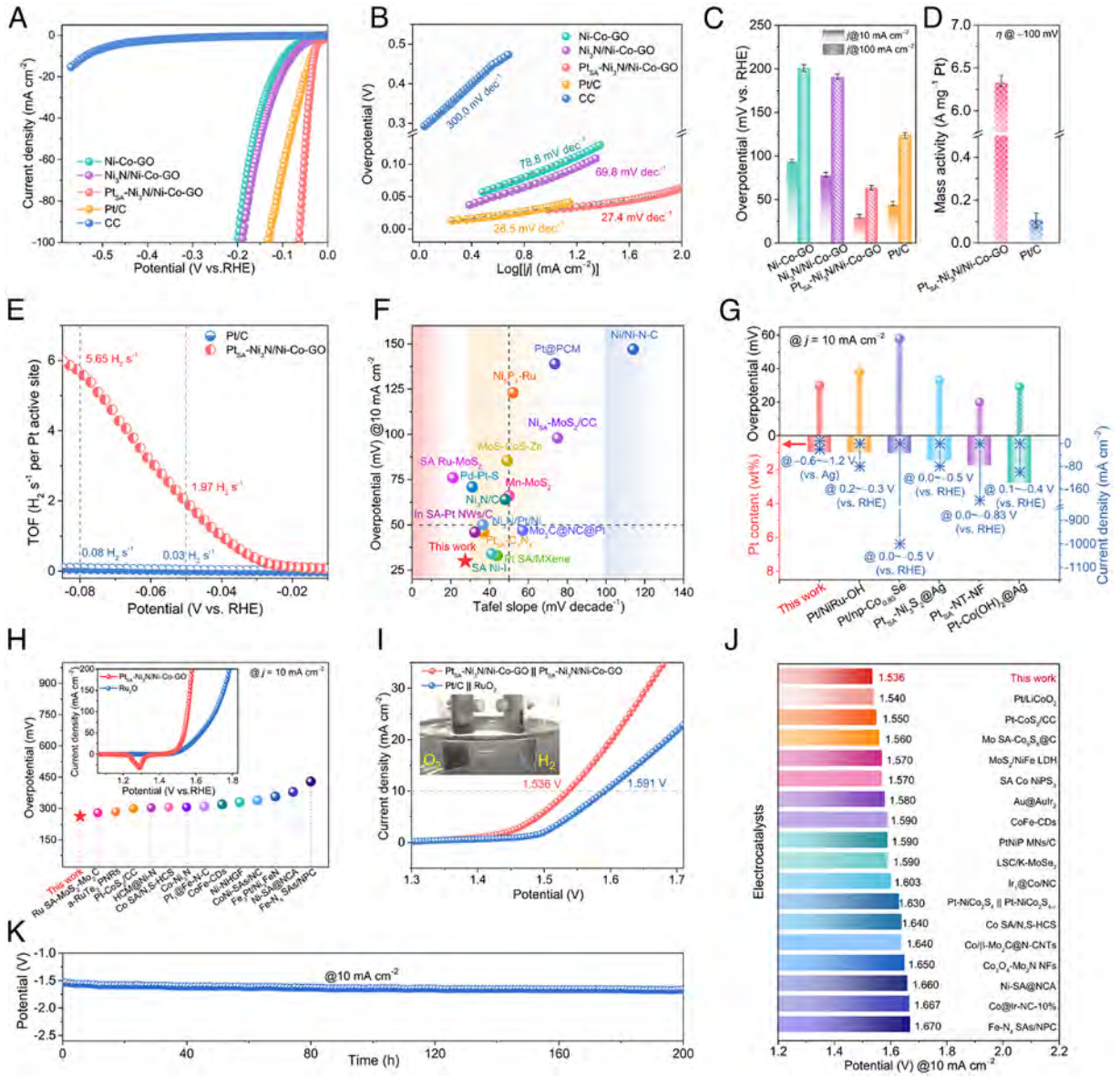

Fig. 4. Alkaline electrocatalytic performance and comparison. (*A*) LSV curves, (*B*) Tafel plots, and (*C*) corresponding overpotentials at 10 and 100 mA cm^{-2} for the Pt_{SA}-Ni_3N/Ni-Co-GO, Ni_3N/Ni-Co-GO, Ni-Co-GO, and Pt/C. (*D*) The mass activity of the Pt_{SA}-Ni_3N/Ni-Co-GO and Pt/C. (*E*) TOFs plots of the Pt_{SA}-Ni_3N/Ni-Co-GO and Pt/C. (*F*) Comparison of Tafel slope and overpotentials (at 10 mA cm^{-2}) with references all measured in 1.0 M KOH. (*G*) Comparison of HER performance, Pt contents, and electrodeposition conditions for Pt_{SA}-Ni_3N/Ni-Co-GO with reported SACs obtained from aqueous electrolytes. (*H*) Comparison of the overpotentials at 10 mA cm^{-2} for Pt_{SA}-Ni_3N/Ni-Co-GO with previously reported values. *Inset* is the OER polarization curves of Pt_{SA}-Ni_3N/Ni-Co-GO and Ru_2O. (*I*) Polarization curves of Pt_{SA}-Ni_3N/Ni-Co-GO and metric catalysts for overall water splitting. *Inset* is the digital photo during the process. (*J*) Comparison of the cell voltages at 10 mA cm^{-2} for Pt_{SA}-Ni_3N/Ni-Co-GO with reported electrocatalysts. (*K*) The water electrolysis stability test for Pt_{SA}-Ni_3N/Ni-Co-GO at 10 mA cm^{-2} for 200 h in 1.0 M KOH. Error bars in (*C*) and (*D*) illustrate the SD of 10 independent samples.

(12)], demonstrating that ionic liquids have certain advantages for the synthesis of efficient SACs.

In addition, the Pt_{SA}-Ni_3N/Ni-Co-GO gives a larger double-layer capacitance (C_{dl}) of 33.9 mF cm^{-2} compared with the Ni_3N/Ni-Co-GO (17.8 mF cm^{-2}), declaring that more active sites were exposed on the catalyst with Pt atoms immobilization (*SI Appendix*, Fig. S58). Besides, only 3.36 Ω of charge transfer resistance (R_{ct2}) between the electrocatalyst and electrolyte was measured for the Pt_{SA}-Ni_3N/Ni-Co-GO catalyst, which is significantly lower than that of Ni_3N/Ni-Co-GO (12.73 Ω), Ni-Co-GO (21.17 Ω) and CC (520.85 Ω) (*SI Appendix*, Fig. S59), suggesting the enhanced HER charge transfer kinetics and the fast Faradaic reaction process. This observation may be attributed to the incorporation of monatomic Pt altering the electronic structure of SAC and the construction of a 3D porous Ni_3N/Ni-Co-GO heterostructure. As reflected in HER catalyzing durability from long-term electrolysis studies (*SI Appendix*, Figs. S60 and S61), only weeny potential changes after 3,000 cycles or 21 h were observed for Pt_{SA}-Ni_3N/Ni-Co-GO, indicating the admirable cycling and long-term stability. All these results confirmed the outstanding stability of Pt_{SA}-Ni_3N/Ni-Co-GO, highlighting the advance by coupling with single Pt atoms in Ni_3N/Ni-Co-GO. Notably, large area electrodes (3 cm × 3 cm, 5 cm × 5 cm) and the 5-metal (Co, Ni, Ir, Pt, and Au) SAC (η_{10} = 13 mV, b = 19.5 mV dec^{-1}) also exhibit excellent HER activities (*SI Appendix*, Figs. S62 and S63), demonstrating the proposed strategy has good universality and extensibility for the electrochemical synthesis of SACs as well as multimetallic SACs with outstanding catalysis performances.

The OER activity of the Pt_{SA}-Ni_3N/Ni-Co-GO was also measured by LSV. The Pt_{SA}-Ni_3N/Ni-Co-GO only delivers an overpotential of 263 mV at 10 mA cm^{-2} and a low Tafel slope

of 61.4 mV dec^{-1}, which is lower than RuO_2 (η_{10} = 295 mV, b = 103.7 mV dec^{-1}) and most of the recently reported electrocatalysts (Fig. 4*H* and *SI Appendix*, Fig. S64 and Table S5). After HER and OER tests, there was no change in the phase of the sample (*SI Appendix*, Fig. S65). Inspired by the excellent activities of the as-synthesized Pt_{SA}-Ni_3N/Ni-Co-GO toward HER and OER, a two-electrode cell was assembled for overall water splitting in 1.0 M KOH by using Pt_{SA}-Ni_3N/Ni-Co-GO as both cathode and anode (Fig. 4*I*). Compared with Pt/C || RuO_2 (1.591 V), the Pt_{SA}-Ni_3N/Ni-Co-GO electrolyzer only requires a cell voltage of 1.536 V to drive current density of 10 mA cm^{-2}. The outstanding electrochemical activity also overmatches the most reported bifunctional electrocatalysts (Fig. 4*J* and *SI Appendix*, Table S6). As expected, the Pt_{SA}-Ni_3N/Ni-Co-GO electrolyzer exhibits significant stability over 200 h test at low current density but less ideal stability under high current density (Fig. 4*K* and *SI Appendix*, Fig. S66), and the enlarged electrode (5 cm × 5 cm) also possesses comparable catalytic performance for overall water splitting (*SI Appendix*, Fig. S60 and Movie S7).

Theoretical Calculation Analysis. To further investigate the electronic structure and catalysis mechanism of the Ni_3N/Ni-Co-GO tailored Pt SAs with insights into the influences of interface engineering and atom doping on the enhanced catalytic activity, the density functional theory (DFT) calculations were studied. Constructing the optimized Pt_{SA} interface-Ni_3N/Ni-Co and Pt_{SA} surface-Ni_3N/Ni-Co models by single Pt atom replacing certain Ni atom (interface and surface) in Ni_3N/Ni-Co heterostructure, the Ni_3N/Ni-Co and Pt_{SA}-Ni_3N-Co models were also built for comparison (Fig. 5 *A* and *C* and *SI Appendix*, Figs. S67 and S69). The negative formation energies of Pt_{SA} surface-Ni_3N/Ni-Co and Pt_{SA} interface-Ni_3N/Ni-Co indicate that it is theoretically possible for Pt single atom doping on the surface and interface of the Ni_3N/Ni-Co heterostructure (*SI Appendix*, Fig. S70 and *Supporting Text 4*). After a Pt atom is immobilized in Ni_3N/Ni-Co heterostructure or Ni_3N-Co, the charge accumulation is primarily distributed around the Pt site to form a local electron-rich region by metal–support coordination (Fig. 5 *B* and *D* and *SI Appendix*, Fig. S71). The electronic interaction involving the electron transfer between Pt SAs and Ni_3N/Ni-Co support, results in charge distribution changes, which is conducive to enhancing the HER kinetics (53, 54). The projected density of states (PDOS) of Pt_{SA}-Ni_3N-Co, Pt_{SA} surface-Ni_3N/Ni-Co, and Pt_{SA} interface-Ni_3N/Ni-Co reveal a higher occupation at the Pt site near the Fermi level compared to Ni_3N/Ni-Co (Fig. 5*E*), indicating their increased intrinsic electrical conductivity and enhanced electron mobility (55). This result demonstrates that the introduction of Pt atom and Ni_3N/Ni-Co heterostructure can effectively improve the total *d*-electron domination of the catalyst, further boosting the activation of H_2O and energetically catalytic performance, which is consistent with the experimental observations (Fig. 4). The *d*-band features of Pt atom in Ni_3N-Co and Ni_3N/Ni-Co coordinated configurations were also investigated. The Ni_3N/Ni-Co loaded Pt atoms (Pt_{SA} interface-Ni_3N/Ni-Co and Pt_{SA} surface-Ni_3N/Ni-Co) have a wider 5*d* band and higher density near the Fermi level than that of Pt_{SA}-Ni_3N-Co (Fig. 5*F*), suggesting that Ni_3N/Ni-Co-coupled Pt molecules induce more free electrons near the Pt site than Pt_{SA}-Ni_3N-Co, which is more beneficial to the adsorption and transfer of H reactants.

For the HER and OER processes in alkaline solutions, it can be seen that the adsorption energy of H_2O ($\Delta G_{H_2O^*}$) plays an important role. As shown in Fig. 5*G*, the $\Delta G_{H_2O^*}$ for Ni_3N/Ni-Co, Pt_{SA}-Ni_3N-Co, Pt_{SA} surface-Ni_3N/Ni-Co, and Pt_{SA} interface-Ni_3N/Ni-Co are −0.02, −0.46, −0.47, and −0.52 eV, respectively. The Pt_{SA} surface-Ni_3N/Ni-Co and Pt_{SA} interface-Ni_3N/Ni-Co display the more negative binding energies than Ni_3N/Ni-Co and Pt_{SA}-Ni_3N-Co, suggesting that the Ni_3N/Ni-Co structure with atomic-level Pt dopant is favorable for the adsorption of H_2O in the Volmer step, which would promote subsequent reactions. Furthermore, the activation energies of water dissociation on Ni_3N/Ni-Co, Pt_{SA}-Ni_3N-Co, Pt_{SA} surface-Ni_3N/Ni-Co, and Pt_{SA} interface-Ni_3N/Ni-Co are 0.88, 0.67, 0.65, and 0.48 eV, respectively (Fig. 5 *H* and *I* and *SI Appendix*, Fig. S72). These results demonstrate that the Pt_{SA} interface-Ni_3N/Ni-Co heterostructure has the lowest energy barrier for water dissociation into *OH and H*, thereby facilitating HER and OER processes. Moreover, the H atom was anchored in the hollow site of the Ni_3N/Ni-Co surface, and the charge density equally distributed on three Ni sites, forming a stable H* adsorption configuration. However, after anchoring Pt atoms, the charge density redistributes on the surface of Pt_{SA}-Ni_3N-Co, Pt_{SA} surface-Ni_3N/Ni-Co, and Pt_{SA} interface-Ni_3N/Ni-Co, and is mainly concentrated near the Pt atoms (*SI Appendix*, Fig. S73), weakening the H* adsorption strength and further improving the HER performance. The free energies of hydrogen adsorption (â^†G_{H^*}) for the Pt_{SA} interface-Ni_3N/Ni-Co (−0.11 eV) and Pt_{SA} surface-Ni_3N/Ni-Co (−0.13 eV) are closer to 0 eV than that of Ni_3N/Ni-Co (−0.38 eV) and Pt_{SA}-Ni_3N-Co (−0.26 eV), indicating the Pt_{SA}-Ni_3N/Ni-Co has weaker hydrogen adsorption capacity and easier to desorb hydrogen, and thus expediting HER dynamics (Fig. 5*J*).

For the OER process, the transition of *OOH from *O is the rate-determining step (Rds) among four steps for Ni_3N/Ni-Co and Pt_{SA} surface-Ni_3N/Ni-Co (*SI Appendix*, Fig. S74). Compared with the Ni_3N/Ni-Co (η = 0.76 V), the Pt_{SA} surface-Ni_3N/Ni-Co is thermodynamically more suitable for OER with a lower overpotential of 0.57 V. The electron-deficient and positively charged Ni/Co species in Pt_{SA}-Ni_3N/Ni-Co-GO possibly facilitate the generation of surface oxide species as discussed before, which act as catalytically active sites for the OER. The addition of Pt SAs is beneficial to the OER of the Pt_{SA}-Ni_3N/Ni-Co-GO catalyst, mainly because Pt SAs adjust the electronic structure of the Ni_3N/Ni-Co-GO support to obtain electron-deficient and positively charged Ni/Co species. These results confirm that the Pt_{SA}-Ni_3N/Ni-Co obtained in an ionic liquid has promising HER and OER catalytic performances.

Discussion

In summary, we proposed and validated a universal strategy to engineer atomic-scale materials by electrochemically transforming bulk metals into single metal atoms in ionic liquids. Twenty monometallic single-atom materials (Mg, Al, V, Cr, Mn, Fe, Co, Ni, Cu, Zn, Mo, Ru, In, Sn, W, Ir, Pd, Ag, Pt, and Au) and a five-metal (Co, Ni, Ir, Pt, and Au) SAC were effectively prepared through this strategy. When 0.98 wt% Pt atoms are anchored onto the self-standing Ni_3N/Ni-Co-GO heterostructure, the resulting Pt_{SA}-Ni_3N/Ni-Co-GO exhibits exceptional HER and OER performances with a pretty low overpotential of 30 and 263 mV at 10 mA cm^{-2}, a smaller Tafel slope of 27.4 and 61.4 mV dec^{-1}, respectively. Moreover, the Pt_{SA}-Ni_3N/Ni-Co-GO@CC coupled in a water electrolyzer only delivers a low cell voltage of 1.536 V to reach 10 mA cm^{-2} for overall water splitting and exhibits significant stability. The successful preparation of bifunctionally amplified electrodes with efficient catalytic activity suggests that the method is promising for industrial applications. Theoretical

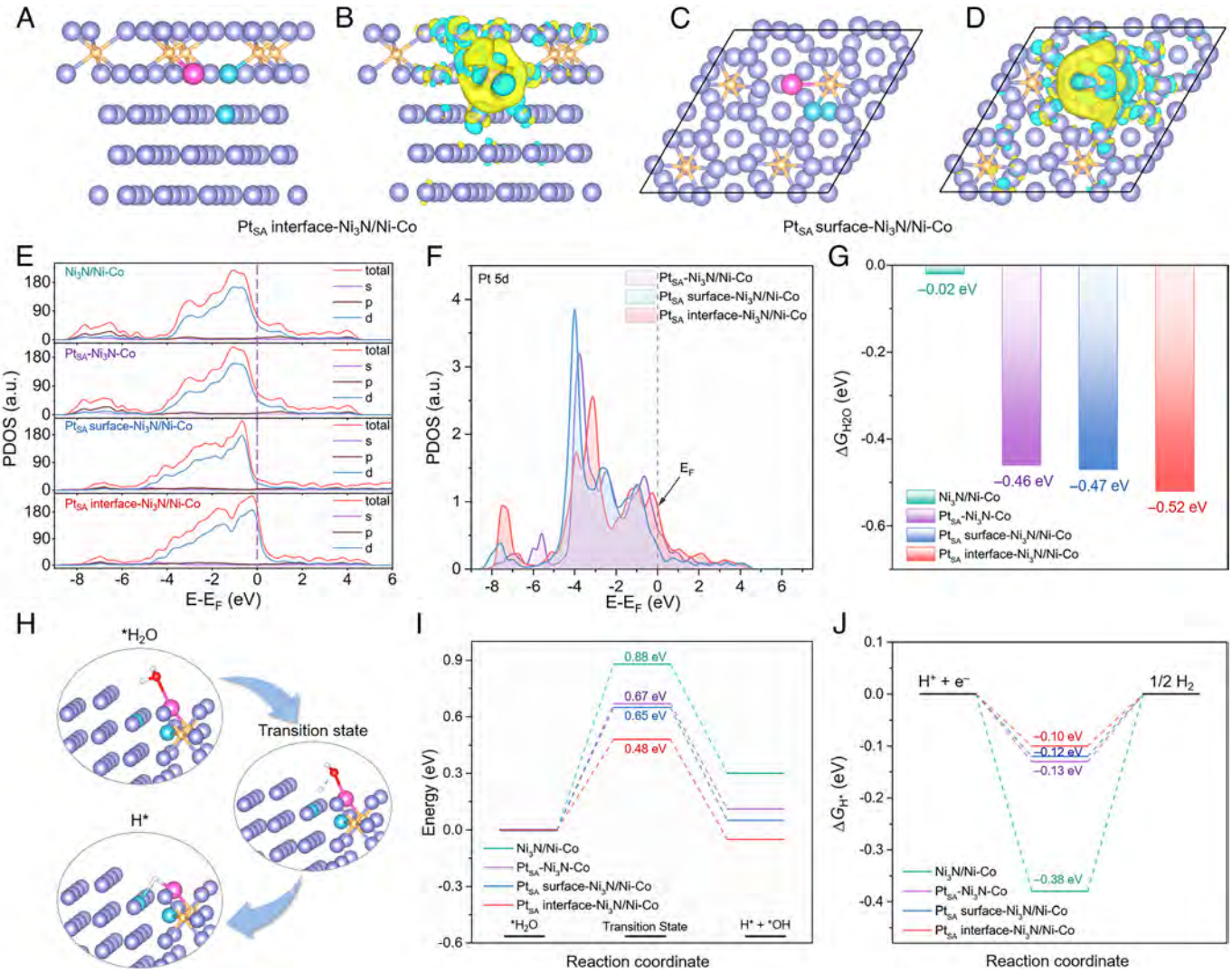

Fig. 5. Theoretical calculation investigations. (*A*) Side view of the optimized structure and (*B*) calculated electron density difference for Pt_{SA} interface-Ni_3N/Ni-Co. (*C*) Top view of the optimized structure and (*D*) calculated electron density difference for Pt_{SA} surface-Ni_3N/Ni-Co. Yellow color represents charge density accumulation, and the cyan areas show charge density reduction (the isosurface value is 0.003 e Å^{-1}). (*E*) Calculated PDOS of Ni_3N/Ni-Co, Pt_{SA}-Ni_3N-Co, Pt_{SA} surface-Ni_3N/Ni-Co, and Pt_{SA} interface-Ni_3N/Ni-Co. (*F*) Calculated Pt 5d band of Pt_{SA}-Ni_3N-Co, Pt_{SA} surface-Ni_3N/Ni-Co, and Pt_{SA} interface-Ni_3N/Ni-Co. (*G*) Calculated H_2O adsorption free energies on Ni_3N/Ni-Co, Pt_{SA}-Ni_3N-Co, Pt_{SA} surface-Ni_3N/Ni-Co, and Pt_{SA} interface-Ni_3N/Ni-Co. (*H*) Optimized configuration of the HER process on the Pt_{SA} interface-Ni_3N/Ni-Co. (*I*) Energy barriers of water dissociation and (*J*) calculated H* adsorption free energies diagrams toward HER on Ni_3N/Ni-Co, Pt_{SA}-Ni_3N-Co, Pt_{SA} surface-Ni_3N/Ni-Co, and Pt_{SA} interface-Ni_3N/Ni-Co, respectively.

calculations further imply that the substitution of Pt atoms for Ni atoms on the surface and interface of this catalyst can modulate its internal electronic structure, contributing to boosting the adsorption and dissociation of H_2O, the desorption of H*, as well as the O–O coupling, which intuitively reflects the superior HER and OER activities. This general strategy enables the synthesis of various single-atom materials, including multimetallic SACs, by designing ionic liquids and support materials. It broadens the pathways for electrochemical synthesis of SACs with the potential for industrialization, and may also expand a direction for the applications of ionic liquids.

Materials and Methods

Raw Materials. All the raw materials, including choline chloride [$HOC_2H_4N(CH_3)_3Cl$], ethylene glycol [$(CH_2OH)_2$], nickel chloride hexahydrate ($NiCl_2{\cdot}6H_2O$), cobalt chloride hexahydrate ($CoCl_2{\cdot}6H_2O$), K_2PtCl_4, graphene oxide (GO), 1-ethyl-3-methylimidazolium tetrafluoroborate, 1-butyl-3-methylimidazolium tetrafluoroborate, urea, potassium hydroxide (KOH), Pt/C (20 wt % Pt), ruthenium dioxide (RuO_2), Nafion solution, Mg, Al, V, Cr, Mn, Fe, Co, Ni, Cu, Zn, Mo, In, Sn and W plate, Ru bulk, Ir wire, and alcohol were purchased from commercial sources and directly used without further purification.

Synthesis of the Pt_{SA}-Ni_3N/Ni-Co-GO@CC. The Pt_{SA}-Ni_3N/Ni-Co-GO@CC was fabricated by the CV method on an electrochemical station (Biologic-803). The three-electrode system consists of the prepared Ni_3N/Ni-Co-GO@CC as a working electrode, Pt plate as a counter electrode, and nonaqueous Ag wire electrode as a reference electrode. Three ionic liquids (ethaline, 1-ethyl-3-methylimidazolium tetrafluoroborate, or 1-butyl-3-methylimidazolium tetrafluoroborate) were used as the electrolytes. The electrochemical synthesis in ethaline electrolyte was carried out from −0.6 to −1.2 V (vs. Ag) at 60 °C with a scan rate of 100 mV s^{-1} for different cycles (500, 1,000, 2,000, 3,000, 4,000, 5,000, 6,000, 8,000, 10,000, and 12,000 cycles). The process was repeated in 1-ethyl-3-methylimidazolium tetrafluoroborate or 1-butyl-3-methylimidazolium tetrafluoroborate electrolyte for 4,000 cycles. As comparisons, the same fabricated procedures were performed in 1.0 M KOH and 1.0 M PBS, respectively, by the CV method at 0 ~ −0.6 V (vs. RHE) for different cycles (6,000, 8,000, 10,000, and 12,000 cycles). Similarly, the fabricated procedures were also conducted in 1.0 and 5.0 M NaCl solutions at 0 ~ −0.6 V (vs. RHE) for 4000 cycles at room temperature, where the Hg/HgO

electrode was used as the reference electrode. The synthesis processes of the Ni-Co-GO@CC, Ni_3N/Ni-Co-GO@CC, Ni_3N-Co-GO@CC, and enlarged Pt_{SA}-Ni_3N/Ni-Co-GO@CC (3 cm × 3 cm and 5 cm × 5 cm) are detailed in *SI Appendix, Supporting Text 5*.

Synthesis of the Pt SAs on Different Supports and M_{SA} (M = Ag, Au, and Pd)-Ni_3N/Ni-Co-GO@CC. The detailed synthesis processes are provided in *SI Appendix, Supporting Text 5*.

Synthesis of the M_{SA} (M = Mg, Al, V, Cr, Mn, Fe, Co, Ni, Cu, Zn, Mo, Ru, In, Sn, W, and Ir)-NG and 5-metal SACs. The nitrogen-doped graphene (NG) powders were fabricated as supported materials (see details in *SI Appendix, Supporting Text 5*). After mixing the NG powders (40 mg) with 0.2 mL Nafion solution (5 wt%), 1.4 mL alcohol, and 0.4 mL deionized water and sonicating, we took 0.6 mL of this liquid and inked it on the CC and then dried it for use as a substrate. The process of preparing SAs is the same as the above method for fabricating Pt_{SA}-Ni_3N/Ni-Co-GO@CC, where Mg, Al, V, Cr, Mn, Fe, Co, Ni, Cu, Zn, Mo, In, Sn or W plate, Ru bulk or Ir wire was replaced to the Pt plate at different conditions (see details in *SI Appendix, Supporting Text 5*). We note that SAs materials with tunable contents can be facilely obtained through adjusting the electrochemical parameters.

Characterizations. X-ray diffraction (XRD) patterns were conducted on a Bruker-AXS D8 Advance with a Cu Kα radiation at a scan rate of 3 ° min^{-1}. The morphology and structure of the as-prepared samples were performed by scanning electron microscopy (SEM, FEI Nova Nano SEM 450) equipped with X-ray energy dispersive spectrometer (EDS, Oxford INCA EDS system) and transmission electron microscope (TEM, FEI TF20) equipped with Super-X EDS. The HAADF-STEM images were obtained on a JEM-ARM300F and Thermo Fisher Scientific Titan Themis Z. The surface elemental analysis was detected by X-ray photoelectron spectra (XPS, Thermo Scientific K-Alpha$^+$). The UPS spectroscopy and the Fourier transform infrared (FTIR) measurements of CO adsorption for catalysts were characterized by PHI5000 Versa Probe III and Tensor 27, respectively. The UV-visible spectra of several solutions were detected by UV-3600. The contents of Pt in the catalysts and solutions were collected by inductively coupled plasma mass spectrometry (ICP-MS, Agilent 7700). The X-ray absorption spectroscopy (XAS) measurements, including X-ray absorption near-edge structure (XANES) and extended X-ray absorption fine structure (EXAFS) of the samples, were performed at the Beamline of TPS44A1 in the National Synchrotron Radiation Research Center (NSRRC), Taiwan, China.

Electrochemical Measurements. Electrochemical tests were examined on a CHI 660e or PARSTAT 4000A electrochemical workstation with a three-electrode system, using Hg/HgO electrode, carbon rod, and the fabricated samples as the reference, counter, and working electrodes, respectively. For comparison, commercial Pt/C (20 wt%) and RuO_2 catalysts inked on CC substrate were also prepared (*SI Appendix, Supporting Text 5*). Except for large-sized electrocatalysts, the geometric surface area of other as-prepared electrocatalysts is 2 cm^2. LSV measurements were performed at a scan rate of 2 mV s^{-1} in 1.0 M KOH solution at room temperature with 95% *iR*-compensations at −0.6 ~ −1.5 V (vs. Hg/HgO) for HER and 0.9 ~ 0.1 V (vs. Hg/HgO) for OER, respectively. In 1.0 M KOH, $E_{RHE} = E_{Hg/HgO} + 0.0591 \times pH + 0.098$ V. The electrochemically active surface areas (ECSAs) were estimated by cyclic voltammetry (CV) with different scan rates (20, 40, 60, 80, 100, and 120 mV s^{-1}) at a potential range of −0.4 ~ −0.5 V (vs. Hg/HgO). AC impedance measurements were evaluated from 5 × 10^5 Hz to 10^{-2} Hz at the overpotential of 100 mV with 5 mV AC voltage. The stability tests and overall water splitting performance tests are detailed in *SI Appendix, Supporting Text 5*.

Theoretical Computational Methods. Spin-polarized DFT calculations were conducted to optimize structures by the Vienna ab initio simulation package (VASP) (56). The projector augmented wave (PAW) potentials with a plane-wave cutoff energy of 450 eV were implemented to compute the interaction between the ionic cores and valence electrons (57, 58). The generalized gradient approximation (GGA) functional of Perdew–Burke–Ernzerhof (PBE) functional was applied as the exchange-correlation functional (59). The Grimme's semiempirical DFT-D3 dispersion correction was utilized to describe the van der Waals (vdW) interactions (60). The convergence criteria of electronic energies and atomic forces for all calculations were 10^{-5} eV and 0.03 eV $Å^{-1}$.

We construct a 4-layered (111) slab structure of Ni_3N from the experimental results as a catalyst surface. A vacuum layer of 15 Å was added to prevent the effects of two adjacent layers. A Ni_3N-Co model was constructed based on the optimized Ni_3N model, and one Ni atom was replaced by Co atom. While the Ni_3N-Co-Pt model was built by replacing two Ni atoms with Co and Pt, respectively. In order to facilitate the establishment of the heterostructure model, the Ni_3N-Ni interface model was constructed by assembling Ni_3N (001) layers with a 2 × 2 supercell onto a 3-layer-thick 4 × 4 Ni (111) slab. During the DFT calculation, the bottom two metal layers were fixed. We applied 4 × 4 × 1 Gamma-centered k-points for the Brillouin zone. To study the HER reaction pathways, the H_2O* and H* absorbed intermediates were optimized by DFT calculation to obtain the energy of each structure. The free energy for H and H_2O adsorption was defined as follows:

$$\Delta G_{H^*} = \Delta E_{H^*} + \Delta ZPE - T\Delta S, \quad [1]$$

$$\Delta G_{H_2O^*} = \Delta E_{H_2O^*} + \Delta ZPE - T\Delta S, \quad [2]$$

where ΔE_{H^*} and $\Delta E_{H_2O^*}$ are calculated adsorption energy of H and H_2O. The zero-point energy (ZPE) and entropy corrections were performed through frequency calculations. We use the computational hydrogen electrode (CHE) model proposed by Nørskov et al. (61) to calculate the Gibbs free energy of the intermediates. The dissociation barrier was computed using the climbing image nudged elastic band (cl-NEB) method (62).

Formation Energy, Quantum Chemistry, and OER Calculations. The calculation details were described in *SI Appendix, Supporting Texts 4 and 5*, respectively.

Data, Materials, and Software Availability. All study data are included in the article and/or supporting information.

ACKNOWLEDGMENTS. We thank the National Natural Science Foundation of China (52022054, 52204317, 51974181, 52374307, and 52334009), the National Key Research and Development Program of China (2022YFC2906100), the Innovation Program of Shanghai Municipal Education Commission (2023ZKZD48), the Science and Technology Commission of Shanghai Municipality (Grant No. 21DZ1208900), the Program for Professor of Special Appointment (Eastern Scholar) at Shanghai Institutions of Higher Learning (TP2019041), and the "Shuguang Program" supported by the Shanghai Education Development Foundation and the Shanghai Municipal Education Commission (21SG42) for financial support.

Author affiliations: [a]State Key Laboratory of Advanced Special Steel and Shanghai Key Laboratory of Advanced Ferrometallurgy and School of Materials Science and Engineering, Shanghai University, Shanghai 200444, China; [b]Key Laboratory of Interfacial Physics and Technology, Shanghai Institute of Applied Physics, Chinese Academy of Sciences, Shanghai 201800, China; [c]Department of Materials Science and Engineering, School of Energy and Environment, City University of Hong Kong, Kowloon Tong, Hong Kong, China; [d]School of Microelectronics, Fudan University, Shanghai 200433, China; [e]Institute of Sustainable Energy, College of Sciences, Shanghai University, Shanghai 200444, China; and [f]Key Laboratory of Applied Chemistry, Yanshan University, Qinhuangdao 066000, China

1. Z. W. Seh *et al.*, Combining theory and experiment in electrocatalysis: Insights into materials design. *Science* **355**, 146 (2017).
2. S. Ji *et al.*, Chemical synthesis of single atomic site catalysts. *Chem. Rev.* **120**, 11900–11955 (2020).
3. X. Zhao, D. He, B. Y. Xia, Y. Sun, B. You, Ambient electrosynthesis toward single-atom sites for electrocatalytic green hydrogen cycling. *Adv. Mater.* **35**, e2210703 (2023).
4. T. Gan, D. Wang, Atomically dispersed materials: Ideal catalysts in atomic era. *Nano Res.* **17**, 18–38 (2023), 10.1007/s12274-022-4371-x.
5. H. Wang *et al.*, Precursor-mediated in situ growth of hierarchical N-doped graphene nanofibers confining nickel single atoms for CO_2 electroreduction. *Proc. Natl. Acad. Sci. U.S.A.* **120**, e2219043120 (2023).
6. H. J. Qiu *et al.*, Nanoporous graphene with single-atom nickel dopants: An efficient and stable catalyst for electrochemical hydrogen production. *Angew. Chem. Int. Ed.* **54**, 14031–14035 (2015).
7. Y. Qu, Z. Li, W. Chen, Y. Lin, Direct transformation of bulk copper into copper single sites via emitting and trapping of atoms. *Nat. Catal.* **1**, 781–786 (2018).

8. B. Qiao *et al.*, Single-atom catalysis of CO oxidation using Pt_1/FeO_x. *Nat. Chem.* **3**, 634–641 (2011).
9. L. Han *et al.*, A single-atom library for guided monometallic and concentration-complex multimetallic designs. *Nat. Mater.* **21**, 681–688 (2022).
10. B. Wang *et al.*, Room-temperature laser planting of high-loading single-atom catalysts for high-efficiency electrocatalytic hydrogen evolution. *J. Am. Chem. Soc.* **145**, 13788–13795 (2023).
11. P. Zhai *et al.*, Engineering single-atomic ruthenium catalytic sites on defective nickel-iron layered double hydroxide for overall water splitting. *Nat. Commun.* **12**, 4587 (2021).
12. K. Jiang *et al.*, Single platinum atoms embedded in nanoporous cobalt selenide as electrocatalyst for accelerating hydrogen evolution reaction. *Nat. Commun.* **10**, 1743 (2019).
13. Z. Zhang *et al.*, Electrochemical deposition as a universal route for fabricating single-atom catalysts. *Nat. Commun.* **11**, 1215 (2020).
14. K. L. Zhou *et al.*, Seamlessly conductive $Co(OH)_2$ tailored atomically dispersed Pt electrocatalyst with a hierarchical nanostructure for an efficient hydrogen evolution reaction. *Energ. Environ. Sci.* **13**, 3082–3092 (2020).
15. M. Zhou, J. E. Dick, A. J. Bard, Electrodeposition of isolated platinum atoms and clusters on bismuth-characterization and electrocatalysis. *J. Am. Chem. Soc.* **139**, 17677–17682 (2017).
16. Z. Wang *et al.*, Electrochemical conversion of bulk platinum into platinum single-atom sites for the hydrogen evolution reaction. *J. Mater. Chem. A* **8**, 10755–10760 (2020).
17. B. J. Plowman, L. A. Jones, S. K. Bhargava, Building with bubbles: The formation of high surface area honeycomb-like films via hydrogen bubble templated electrodeposition. *Chem. Commun.* **51**, 4331–4346 (2015).
18. Y. He, Y. Cui, W. Shang, Z. Zhao, P. Tan, Insight into potential oscillation behaviors during Zn electrodeposition: Mechanism and inspiration for rechargeable Zn batteries. *Chem. Eng. J.* **438**, 135541 (2022).
19. W. L. Tsai *et al.*, Building on bubbles in metal electrodeposition. *Nature* **417**, 139 (2002).
20. M. Asnavandi, C. Zhao, Hydrogen bubble-assisted electrodeposition of metal nanoparticles from protic ionic liquids for electrocatalysis. *ACS Sustain. Chem. Eng.* **5**, 85–89 (2016).
21. A. P. Abbott, G. Frisch, K. S. Ryder, Electroplating using ionic liquids. *Annu. Rev. Mater. Res.* **43**, 335–358 (2013).
22. T. Torimoto, T. Tsuda, K. Okazaki, S. Kuwabata, New frontiers in materials science opened by ionic liquids. *Adv. Mater.* **22**, 1196–1221 (2010).
23. M. P. Singh, R. K. Singh, S. Chandra, Ionic liquids confined in porous matrices: Physicochemical properties and applications. *Prog. Mater. Sci.* **64**, 73–120 (2014).
24. K. Dong, X. Liu, H. Dong, X. Zhang, S. Zhang, Multiscale studies on ionic liquids. *Chem. Rev.* **117**, 6636–6695 (2017).
25. H. Weingartner, Understanding ionic liquids at the molecular level: Facts, problems, and controversies. *Angew. Chem. Int. Ed.* **47**, 654–670 (2008).
26. C. D. Hubbard, P. Illner, R. van Eldik, Understanding chemical reaction mechanisms in ionic liquids: Successes and challenges. *Chem. Soc. Rev.* **40**, 272–290 (2011).
27. S. Ding *et al.*, Electrostatic stabilization of single-atom catalysts by ionic liquids. *Chem* **5**, 3207–3219 (2019).
28. B. B. Hansen *et al.*, Deep eutectic solvents: A review of fundamentals and applications. *Chem. Rev.* **121**, 1232–1285 (2021).
29. J. Wu *et al.*, Deep eutectic solvents for boosting electrochemical energy storage and conversion: A review and perspective. *Adv. Funct. Mater.* **31**, 2011102 (2021).
30. S. J. Wang *et al.*, Unraveling the dissolution mechanism of platinum and silver electrodes during composite electrodeposition in a deep eutectic solvent. *J. Mater. Chem. A* **8**, 4354–4361 (2020).
31. C. Zhong *et al.*, A review of electrolyte materials and compositions for electrochemical supercapacitors. *Chem. Soc. Rev.* **44**, 7484–7539 (2015).
32. P. Jaumaux *et al.*, Non-flammable liquid and quasi-solid electrolytes toward highly-safe alkali metal-based batteries. *Adv. Funct. Mater.* **31**, 2008644 (2020).
33. C. Lagrost, D. Carrie', M. Vaultier, P. Hapiot, Reactivities of some electrogenerated organic cation radicals in room-temperature ionic liquids: Toward an alternative to volatile organic solvents? *J. Phys. Chem. A* **107**, 745–752 (2003).
34. B. Xi, X. Sun, Single-atom catalysts electrostatically stabilized by ionic liquids. *Chem* **5**, 3012–3014 (2019).
35. X. Zhang *et al.*, A stable low-temperature H_2-production catalyst by crowding Pt on α-MoC. *Nature* **589**, 396–401 (2021).
36. W. Ni *et al.*, Ni_3N as an active hydrogen oxidation reaction catalyst in alkaline medium. *Angew. Chem. Int. Ed.* **58**, 7445–7449 (2019).
37. S. Nandi *et al.*, Low band gap benzimidazole COF supported Ni_3N as highly active OER catalyst. *Adv. Energy Mater.* **6**, 1601189 (2016).
38. S. Ye *et al.*, Highly stable single Pt atomic sites anchored on aniline-stacked graphene for hydrogen evolution reaction. *Energ. Environ. Sci.* **12**, 1000–1007 (2019).
39. C. Li *et al.*, Polyvinylpyrrolidone-coordinated single-site platinum catalyst exhibits high activity for hydrogen evolution reaction. *Angew. Chem. Int. Ed.* **59**, 15902–15907 (2020).
40. P. Kuang *et al.*, Pt single atoms supported on N-doped mesoporous hollow carbon spheres with enhanced electrocatalytic H_2-evolution activity. *Adv. Mater.* **33**, e2008599 (2021).
41. X. Huang *et al.*, High-performance transition metal-doped Pt_3Ni octahedra for oxygen reduction reaction. *Science* **348**, 1230–1234 (2015).
42. S. Fang *et al.*, Uncovering near-free platinum single-atom dynamics during electrochemical hydrogen evolution reaction. *Nat. Commun.* **11**, 1029 (2020).
43. S. Yang, Y. J. Tak, J. Kim, A. Soon, H. Lee, Support effects in single-atom platinum catalysts for electrochemical oxygen reduction. *ACS Catal.* **7**, 1301–1307 (2017).
44. Z. Zhang *et al.*, Thermally stable single atom Pt/m-Al_2O_3 for selective hydrogenation and CO oxidation. *Nat. Commun.* **8**, 16100 (2017).
45. K. Ding *et al.*, Identification of active sites in CO oxidation and water-gas shift over supported Pt catalysts. *Science* **350**, 189–192 (2015).
46. Z. Lv *et al.*, Co-constructing interfaces of multiheterostructure on MXene ($Ti_3C_2T_x$)-modified 3D self-supporting electrode for ultraefficient electrocatalytic HER in alkaline media. *Adv. Funct. Mater.* **31**, 2102576 (2021).
47. Q. Fu *et al.*, 2D Transition metal dichalcogenides: Design, modulation, and challenges in electrocatalysis. *Adv. Mater.* **33**, e1907818 (2021).
48. H. Zhang *et al.*, Dynamic traction of lattice-confined platinum atoms into mesoporous carbon matrix for hydrogen evolution reaction. *Sci. Adv.* **4**, eaao6657 (2018).
49. X. Peng *et al.*, Heteroatom coordination induces electric field polarization of single Pt sites to promote hydrogen evolution activity. *Nanoscale* **13**, 7134–7139 (2021).
50. Z. Li *et al.*, Iridium single-atom catalyst on nitrogen-doped carbon for formic acid oxidation synthesized using a general host-guest strategy. *Nat. Chem.* **12**, 764–772 (2020).
51. D. Li *et al.*, An effective hybrid electrocatalyst for the alkaline HER: Highly dispersed Pt sites immobilized by a functionalized NiRu-hydroxide. *Appl. Catal. B: Environ.* **269**, 118824 (2020).
52. L. Zhang, L. Han, H. Liu, X. Liu, J. Luo, Potential-cycling synthesis of single platinum atoms for efficient hydrogen evolution in neutral media. *Angew. Chem. Int. Ed.* **56**, 13694–13698 (2017).
53. K. L. Zhou *et al.*, Atomically dispersed platinum modulated by sulfide as an efficient electrocatalyst for hydrogen evolution reaction. *Adv. Sci.* **8**, 2100347 (2021).
54. R. Li, D. Wang, Understanding the structure-performance relationship of active sites at atomic scale. *Nano Res.* **15**, 6888–6923 (2022).
55. K. L. Zhou *et al.*, Platinum single-atom catalyst coupled with transition metal/metal oxide heterostructure for accelerating alkaline hydrogen evolution reaction. *Nat. Commun.* **12**, 3783 (2021).
56. G. Kresse, J. Furthmüller, Efficient iterative schemes for ab initio total-energy calculations using a plane-wave basis set. *Phys. Rev. B* **54**, 11169–11186 (1996).
57. P. E. Blöchl, Projector augmented-wave method. *Phys. Rev. B* **50**, 17953–17979 (1994).
58. D. Joubert, From ultrasoft pseudopotentials to the projector augmented-wave method. *Phys. Rev. B* **59**, 1758–1775 (1999).
59. I. G. McKendry *et al.*, Redox properties of birnessite from a defect perspective. *Proc. Natl. Acad. Sci. U.S.A.* **114**, 9523–9528 (2017).
60. S. Grimme, J. Antony, S. Ehrlich, H. Krieg, A consistent and accurate ab Initio parametrization of density functional dispersion correction (DFT-D) for the 94 elements H-Pu. *J. Chem. Phys.* **132**, 154104 (2010).
61. J. K. Nørskov *et al.*, Origin of the overpotential for oxygen reduction at a fuel-cell cathode. *J. Phys. Chem. B* **108**, 17886–17892 (2004).
62. G. Henkelman, B. P. Uberuaga, H. Jo´nsson, A climbing image nudged elastic band method for finding saddle points and minimum energy paths. *J. Chem. Phys.* **113**, 9901–9904 (2000).